Supporting Information

Thermomechanically stable supramolecular elastomers inspired by heat shock proteins

Qi Wu[1], Hui Liu[1], Hui Xiong[1], Yujia Hou[1], Yan Peng[1], Lijuan Zhao[2], and Jinrong Wu[1]*

1. State Key Laboratory of Polymer Materials Engineering, College of Polymer Science and Engineering, Sichuan University, Chengdu, 610065, China.

2. College of Chemistry and Materials Science, Sichuan Normal University, Chengdu, 610066, China

* Corresponding author: wujinrong@scu.edu.cn (J. Wu).

Materials and Methods

Materials:

Butyl acrylate (BA), 1-vinylimidazole (VI), 2,2'-azobis-(isobutyronitrile) (AIBN) and 1,4-phenylenediboronic acid (PDBA) were provided by TCI (shanghai) Development Co. Ltd. Polystyrene-block-polybutadiene-block-polystyrene (SBS, styrene 30 wt%) were supplied by Sigma-Aldrich. Carbon nanotubes (CNT, NanocylTM NC7000) was purchased from Nanocyl SA, Belgium. 1-Ethylimidazole, ethyl acetate, hexane, ethanol, and tetrahydrofuran (THF) were obtained by Admas Reagent, Ltd. The chemicals were used as received except BA, which were filtrated through a basic alumina column to remove the inhibitor.

Synthesis:

Preparation of butyl acrylate/vinylimidazole copolymer (P(BA-*co*-VI))

P(BA-*co*-VI) was synthesized by free-radical copolymerization of BA and VI. In a typical process, BA (5 g, 0.039 mol), VI (0.262 g, 2.78 mmol) and AIBN (6.8 mg, 0.041 mmol) were dissolved in ethyl acetate (10 mL). The mixture was bubbled with argon gas for 1 h and then heated at 70 ^{o}C for 8 h under argon atmosphere. The resulting product was precipitated in hexane for at least three times. Finally, the product was dried at 40 ^{o}C in a vacuum oven to constant weight. P(BA-*co*-VI) samples varying with the feed molar ratios of BA and VI were accomplished in the same way. The synthetic scheme and results are shown in Scheme S1 and Table S1, respectively.

Preparation of thermomechanically stable supramolecular elastomers (TSEs)

TSEs were formed by doping PDBA into P(BA-*co*-VI) with the equivalent mole ratio between boron centers and imidazole ligands. Typically, P(BA-*co*-VI) (5 g) was dissolved in THF/ethanol (v/v, 1 : 1, 30 mL), and then the desired molar ratio of PDBA was added into the above solution. The resulting mixture was poured into a Teflon mold. After the solvent was slowly evaporated, the resulting film was put in the vacuum oven at 40 ^{o}C for 24 h.

Preparation of SBS film

SBS film was obtained by compression molding at 115 °C for 15 min.

Fabrication of CNT-doped elastomers

TSE-9/CNT was fabricated by dispersing CNT in TSE-9 followed by film-forming process. 5 g TSE-9 was dissolved in THF/ethanol (v/v, 1 : 1, 25 mL), and then 0.25 g CNT was added into the above solution. The resulting mixture was poured into a Teflon mold. After the solvent was slowly evaporated, the resulting film was put in the vacuum oven at 40 ^{o}C for 24 h. HiSHE-37/CNT was fabricated by the same method where the weight ratio of CNT to HiSHE-37 is 5%.

Measurements and methods

Fourier transform infrared spectroscopy (FTIR): FTIR spectra were recorded by using a Thermo Scientific Nicolet iS50 FTIR by an attenuated total reflection mode for at room temperature. Temperature dependent FTIR spectra were obtained by the transmission mode at the temperature from 30 to 150 °C. The wavenumber scale was from 4000 cm^{-1} to 500 cm^{-1}.

Raman spectroscopy: Micro-Raman spectra was performed using a LabRAM HR Evolution micro-Raman spectrometer (HORIBA Jobin Yvon) equipped with 532 nm laser source. Temperature dependent Raman spectra were obtained at the temperature from 25 to 150 °C.

Proton nuclear magnetic resonance (^{1}H NMR): ^{1}H NMR spectra were measured by a Bruker AV III HD 400 MHz spectrometer. CD_3OD (δ (^{1}H) = 3.31 ppm) was used as the solvent. The actual VI/BA molar ratio of the final products was calculated by the molar ratio of imidazole protons to

methyl protons. Temperature dependent ^{1}H NMR spectra were recorded by a Bruker AV II 400 MHz spectrometer. Dimethyl sulfoxide-d6 (DMSO-d6, δ (^{1}H) = 2.50 ppm) was used as the solvent.

Boron-11 nuclear magnetic resonance (^{11}B NMR): ^{11}B NMR spectra were measured by a Bruker AV II-600 MHz spectrometer. Boronic acid was used as the standard. Temperature dependent ^{11}B NMR spectra were recorded by a Bruker AV II-600 MHz spectrometer. Dimethyl sulfoxide-d6 was used as the solvent.

Thermal gravimetric analysis coupled with mass spectroscopy (TGA-MS): TGA-MS spectra were carried out on a NETZSCH STA449 F3 thermal gravimetric analyzer coupled with a QMS 403 Aëolos® Quadro mass spectrometer. The sample was heated from 30 to 300 °C at the heating rate of 10 °C/min under argon atmosphere with a flow rate of 50 mL/min. The mass scan range of generated volatiles was selected to be 1–100 amu with a scan-rate of 200 ms/amu.

High performance liquid chromatography (HPLC): HPLC analyses were worked on an Agilent LC1290 with 254 nm UV detection. The heat-treated sample is putting PDBA in 150 °C for 30 min followed by returning and storing at room temperature.

Gel permeation chromatography (GPC): The molecular weight was measured by a Tosoh HIC-8320GPC with THF as the eluent.

Thermal gravimetric analyzer (TGA): TGA curves were measured by TA Q500. The sample was heated from 25 to 800 °C at the heating rate of 10 °C/min under nitrogen atmosphere with a flow rate of 25 mL/min.

Differential scanning calorimeter (DSC): Heat flow curves were obtained on TA Q2000. The sample was firstly heated from 25 to 130 °C and then cooled from 130 to -70 °C at a cooling rate of 20 °C/min to eliminate the thermal history. Afterwards, the heat flow was recorded from -70 to 130 °C at a heating rate of 10 °C/min.

Dynamic mechanical analysis (DMA): Dynamic mechanical properties were measured on TA Q800 in a tension mode. The rectangle samples with 20 mm in length, 5 mm in width, about 1 mm in thickness were heated from -50 to 200 °C at a heating rate of 3 °C/min. Dynamic mechanical properties were acquired using a frequency of 1 Hz and a preload force of 0.01 N. The dynamic mechanical properties with repeated heat treatment were also carried on TA Q800 in a tension mode. The sample was firstly heated from -50 to 150 °C at a heating rate of 3 °C/min and then cooled from 150 to -50 °C at a cooling rate of 10 °C/min, finally heated from -50 to 150 °C at a heating rate of 3 °C/min.

Rheological measurement: The rheological behaviors were carried out on Anton Paar MCR302 rheometer using a parallel plate of 8 mm diameter. Samples were prepared in the form of disks with a diameter of 8 mm and a thickness of 1 mm. Frequency sweeps were performed from 0.01 to 50 Hz with a constant strain of 0.1% at 25 °C. Frequency sweeping from 0.1 to 50 Hz with a strain of 0.1 % were conducted at 20, 40, 60, 80, 100, 120, 140, 160, 180 °C, respectively. Master curves of P(BA-*co*-VI) were obtained by shifting the frequency sweeping curves at different temperatures to 20 °C.

Scanning electron microscope (SEM): The samples were cut into two pieces by a blade followed by contacting the fracture, then the fracture was wetted by ethyl acetate and contacted together, then the healing process of the fracture observed by the SEM (Nova nanoSEM450) at room temperature.

Tensile test: Tensile experiments were performed on a Instron 5967 tensile tester. The samples were cut into a dumbbell shape with a gauge length of 15 mm, a width of 2 mm, and a thickness of 1mm. Uniaxial tensile measurements were carried out in air at room temperature with strain rates

of 0.011, 0.055, 0.111 and 0.277 s^{-1}, respectively. Temperature dependent uniaxial tensile measurements were obtained in air at the strain rate of 0.055 s^{-1} with temperatures of 25, 50, 75, 100, 120 ^{o}C, respectively. Cyclic tensile tests were also performed on the same machine. The samples were firstly stretched by a loading cycle to the constant strain with the speed of 0.055 s^{-1} and then unloaded at the same rate. The following cyclic tests were performed with 3 min resting after every unloading.

Electrical measurements: Electrical measurements were performed on a Keithley 6487 in a resistance mode. The set voltage and electric current were 1 V and 25 mA, respectively. The data of resistance versus time were recorded by the software of Keithley 6487 test system.

Theoretical calculation based on density functional theory (DFT): The boron dative bond energies for PDBA/1-ethylimidazole model and boroxane/1-ethylimidazole model were evaluated. All calculations in this work were performed using Gaussian 09 program package (Gaussian 09 (Revision D.01), I. Gaussian, Wallingford, CT, 2013). Full geometry optimizations in water were performed to locate all the stationary points, using M062X[1]/def2tzvp[2, 3]. Harmonic vibrational frequency was performed at the same level to guarantee that there is no imaginary frequency in the molecules, i.e., they locate on the minima of potential energy surface. Natural bond orbital (NBO) of all optimized structures were performed to obtain further insight into the electronic properties.[4]

Self-healing efficiency: The self-healing properties were quantified by comparing the fracture strain of the pristine sample and the restored sample, as follows:

$$Healing\ efficiency = \frac{\varepsilon_{cut}}{\varepsilon_{uncut}}$$

Where the ε_{cut} stands for the fracture strain of the cut sample and ε_{uncut} stands for the fracture strain of the uncut sample.

Additional discussion

Detailed discussion of PDBA upon temperature

1. The temperature dependent FTIR spectra

There are no obvious B_3O_3 peaks with temperature increasing, indicating that no distinct formation of boroxines (Fig. S1).[5]

2. The temperature dependent Raman spectra

The peaks in the region of 3000-3100 cm^{-1} are assigned to aromatic C-H vibrations of PDBA.[6]

3. The temperature dependent ^{11}B NMR spectra

The peak around 0 ppm corresponds to a four-coordinated boron environment, which demonstrates that dative bonding occurs via boron centers and oxygen atoms. The peak between 20 and 30 ppm corresponds to a three-coordinated boron environment.[7, 8]

As temperature goes up, the decreasing peak around 0 ppm means the reduction of the proportion of four-coordinated boron centers, indicating that the dative bonds between boron atoms and oxygen atoms break with heat treatment.

4. The temperature dependent ^{1}H NMR spectra

The chemical shift of hydroxyl group in PDBA is around 3.3 ppm at room temperature.[9] With increasing temperature, the shift of B-OH protons from 3.3 to 2.8 ppm[10] and the slight chemical shifts of signals of aromatic protons (8.28 and 7.45 ppm) [11, 12] are observed, which are similar to those reported in the literature for phenylboronic acid derivatives with B-O-B species, suggesting the formation of boroxanes via condensation of phenylboronic acid.

5. TGA-MS spectra of PDBA

The theoretical calculation of completely dehydration reactions of PDBA is that one molecule of PDBA can totally loss two molecules of H_2O:

$$The\ mass\ loss = \frac{Two\ molecules\ of\ H_2O}{One\ molecule\ of\ PDBA} = \frac{18.02 \times 2}{165.75} = 21.7\%$$

The actual mass loss is similar to the calculated mass loss in TGA-MS.

In conclusion, the mass loss of 20.2% and the H_2O fragments (m/z = 16-18) confirm the dehydration reaction of PDBA.

FTIR and ^{1}H NMR spectra of P(BA-*co*-VI)

The appearance of imidazole C=C–H/N=C–H stretching (3111 cm^{-1}), C=N ring stretching (1492 cm^{-1}) and imidazole ring vibration (1225 cm^{-1}) on FTIR spectra and meanwhile the presence of imidazolic protons between 6.8 and 7.7 ppm on ^{1}H NMR spectra suggest the successful introduction of imidazole groups onto the main chains (Fig. 3a and S7).[13, 14] In the ^{1}H NMR spectra of P(BA-*co*-VI), the CH_2 protons near to oxygen atom absorb at 4.08 ppm; The aliphatic protons absorb at 1.2-2.4 ppm; The CH_3 protons absorb at 0.98 ppm.[15]

Detailed structural discussion of TSEs

FTIR measurements of TSEs show that the imidazole C=C–H/N=C–H stretching, C=N ring stretching and imidazole ring vibration are shifted to higher wavenumbers of 3140, 1506 and 1236 cm^{-1} respectively, indicating that the rigidity of imidazole ring increases because of the boron/imidazole dative bonds (Fig. 3a).

Due to the formation of dative bonds, PDBA can be dispersed homogeneously in the film, which is confirmed by the high optical transmittance around 80% in the visible region (Fig. S8).[16] TGA measurements exhibit that the TSEs with more cross-linking ligands show higher thermal stability than that of P(BA-*co*-VI) (Fig. S10).

Comparation between PDBA/imidazole dative model and boroxane/imidazole dative model

^{11}B NMR spectra with different temperature are performed on PDBA (1 equiv.) with 1-ethylimidazole (2 equiv.) in DMSO-d6 solvent (Fig. S13). The imidazole-coordinated (four-coordinated) boron centers are still in the majority with increasing temperature, indicating that the dehydrated boroxanes can stabilize the boron dative bonding at high temperature.

Mechanical properties of TSEs

As shown in Figure 4a, increasing the molar contents of boron atoms and imidazole groups, the tensile strengths are 3.5 MPa for TSE-4, 7.7 MPa for TSE-9, and 14.6 MPa for TSE-15, meanwhile the corresponding ruptured strains are 740% for TSE-4, 490% for TSE-9, and 9% for TSE-15. These results indicate that TSEs can be easily tuned from soft state to plastic-like state by changing the crosslinking density caused by the molar contents of boron atoms and imidazole groups.[17]

Rheological properties of TSEs

Rheological measurements are performed on TSE-9 and P(BA-*co*-VI). Dynamic mechanical properties as a function of frequency ranging from 0.01 to 50 Hz are shown in Fig. S19a. The moduli of TSE-9 are much higher than those of P(BA-*co*-VI), indicating that PDBA-crosslinked network can greatly improve the elastic properties. Frequency sweeps with different temperatures of TSE-9 are shown in Fig. S19b. The storage modulus (G′) is always higher than the loss modulus (G″) in the whole temperature range, demonstrating that TSE-9 exhibit elastic properties even in high temperatures. The master curves of P(BA-*co*-VI) are shown in Fig. S19c. The terminal flow can be

observed in P(BA-*co*-VI).

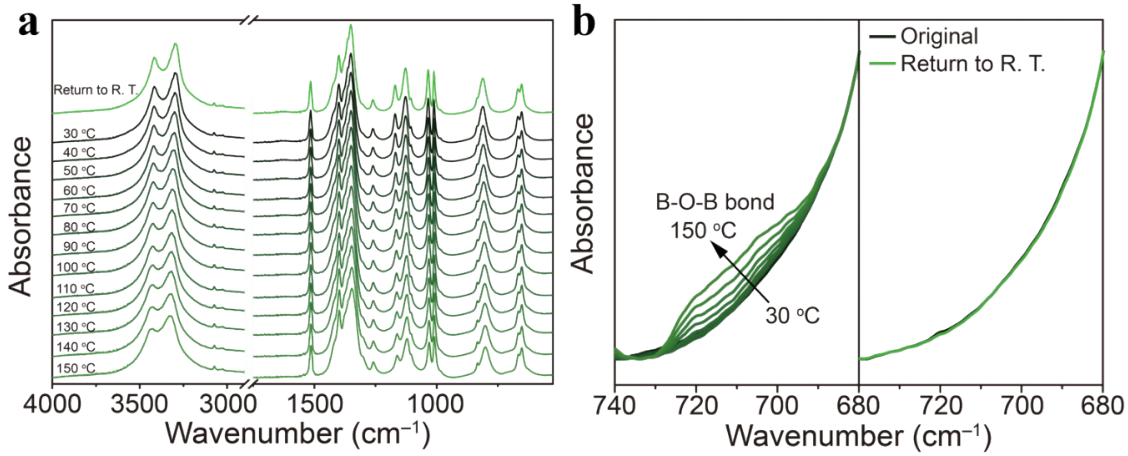

Figure S1. (a) The temperature dependent FTIR spectra of PDBA. (b) The temperature dependent FTIR spectra of PDBA from 1520 to 1480 cm^{-1} (left) and FTIR spectra of PDBA returned to room temperature and the original PDBA (right).

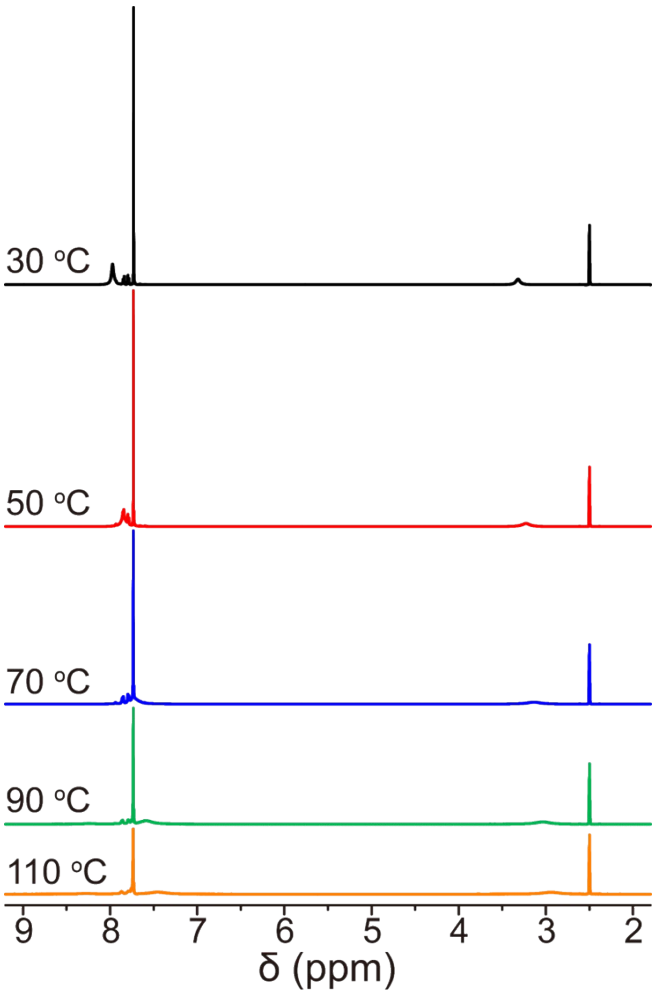

Figure S2. The temperature dependent ^{1}H NMR spectra of PDBA.

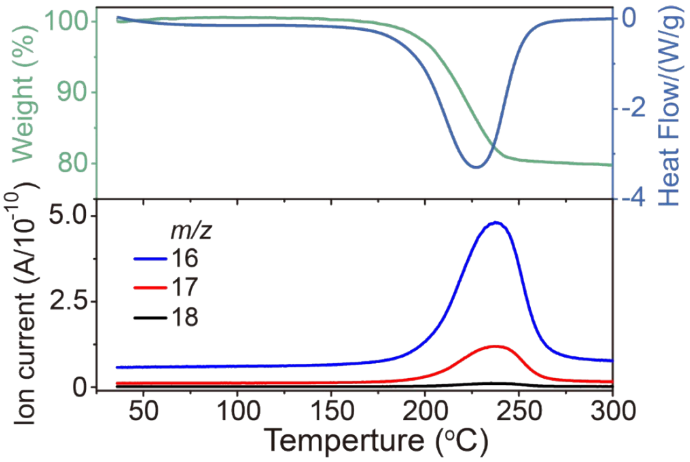

Figure S3. TGA-MS spectra of PDBA.

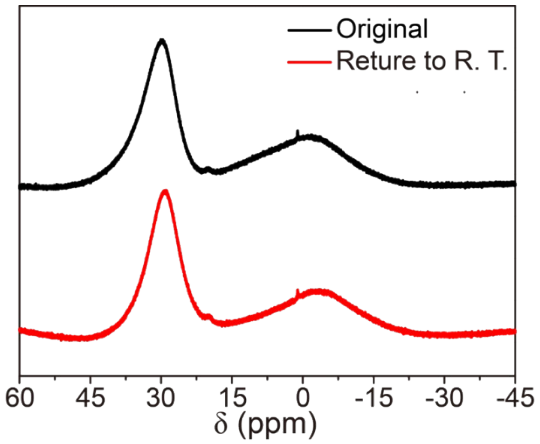

Figure S4. ^{11}B NMR spectra of PDBA returned to room temperature and the original PDBA.

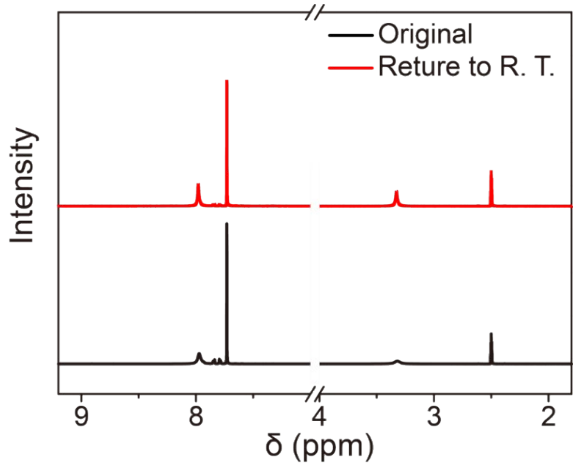

Figure S5. ^{1}H NMR spectra of PDBA returned to room temperature and the original PDBA.

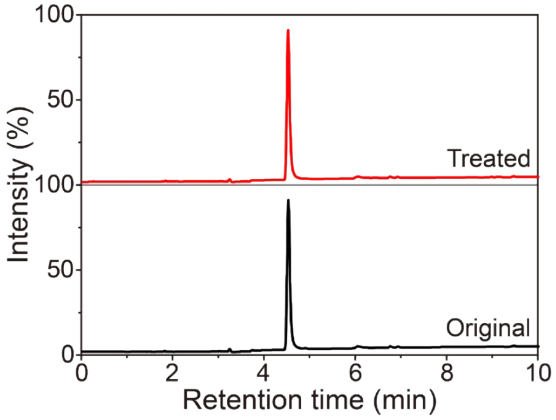

Figure S6. HPLC spectra of PDBA: The same retention times of the heat-treated and original PDBA indicate the full restoration of PDBA when returning to room temperature.

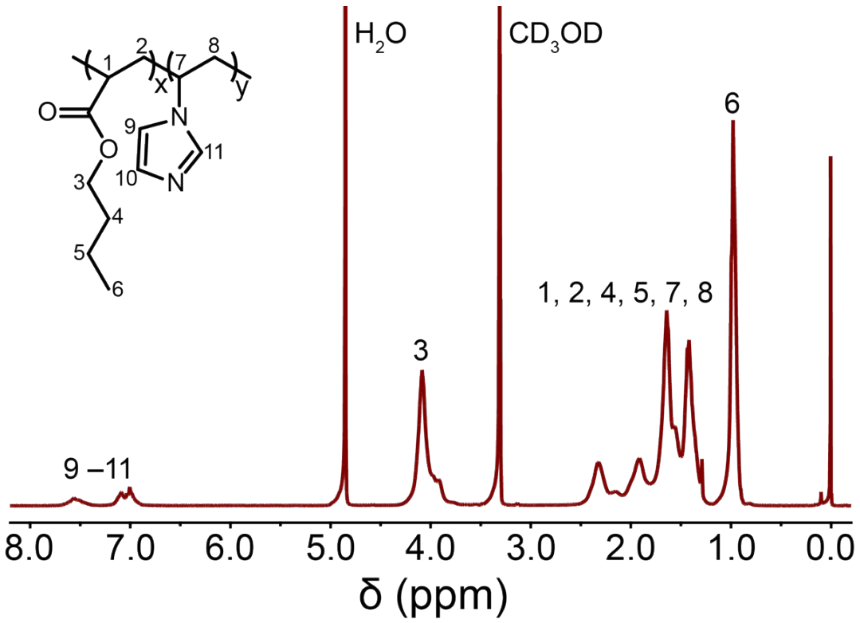

Figure S7. [1]H NMR spectrum of P(BA-*co*-VI).

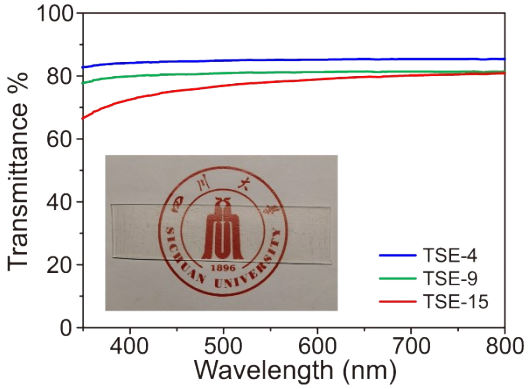

Figure S8. Transmittance spectra of TSEs: The high optical transmittance (over 80%) confirms that PDBA can be dispersed homogeneously in the film.

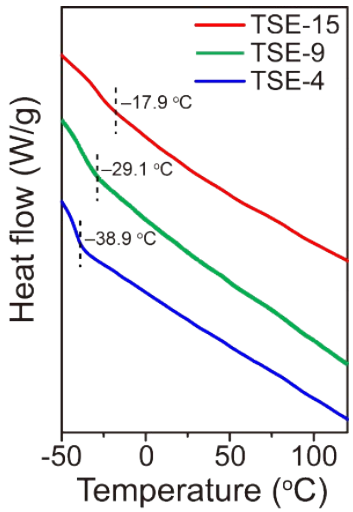

Figure S9. DSC curves of TSEs.

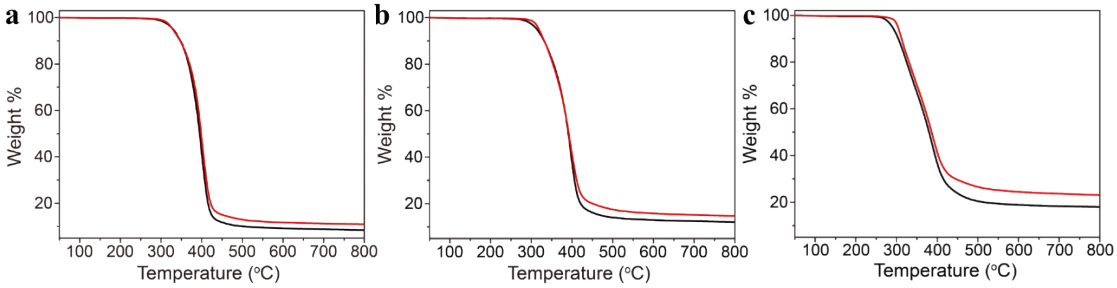

Figure S10. TGA curves for P(BA-*co*-VI) (black lines) and the corresponding TSE-*n* (red lines): TSE-4 (a), TSE-9 (b), and TSE-15 (c).

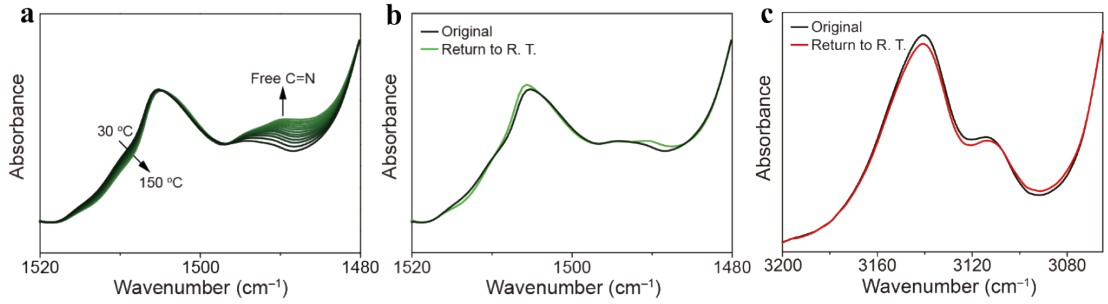

Figure S11. (a) The temperature dependent FTIR spectra from 1520 to 1480 cm^{-1}. (b) FTIR spectra of TSE-9 returned to room temperature and the original TSE-9 from 1520 to 1480 cm^{-1}. (c) FTIR spectra of TSE-9 returned to room temperature and the original TSE-9 from 3200 to 3060 cm^{-1}.

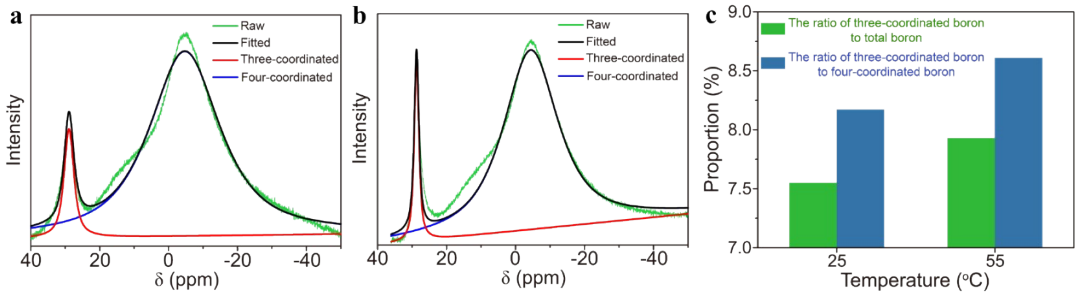

Figure S12. The ^{11}B NMR spectra of TSE-9 in DMF-d6/MeOH-d4 solvent at 25 °C (a) and 55 °C (b). The proportion of three-coordinated boron centers in 25 and 55 °C (c). With increasing temperatures from 25 to 55 °C, the ratio of three-coordinated boron centers to total boron centers increases from 7.5% to 7.9%, demonstrating the rupture of boron/nitrogen dative bonds and the conversion of four-coordinated boron centers to three-coordinated boron centers.

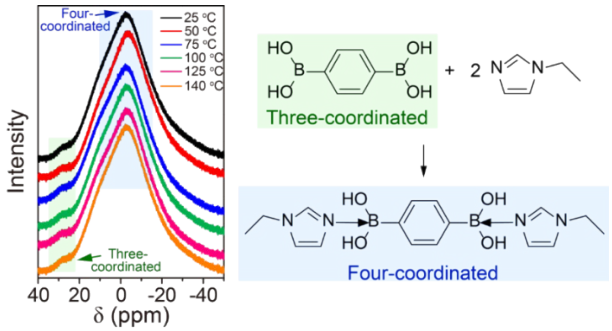

Figure S13. Temperature dependent ^{11}B NMR spectra of PDBA (1 equiv.)/1-ethylimidazole (2 equiv.) model (DMSO-d6).

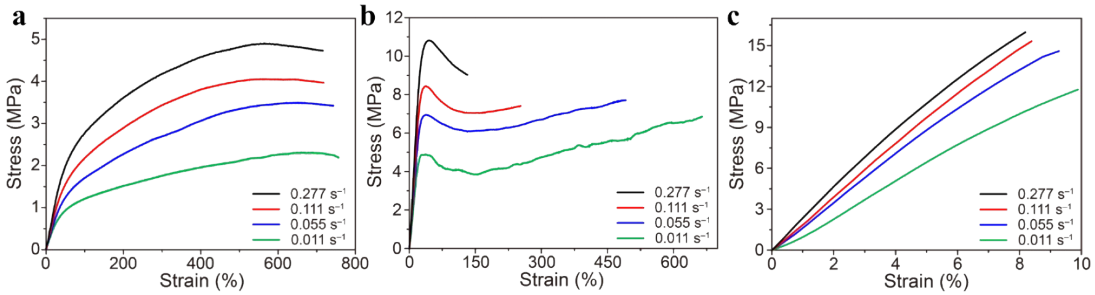

Figure S14. Stress-strain curves with different stain rates of TSE-4 (a), TSE-9 (b), and TSE-15 (c).

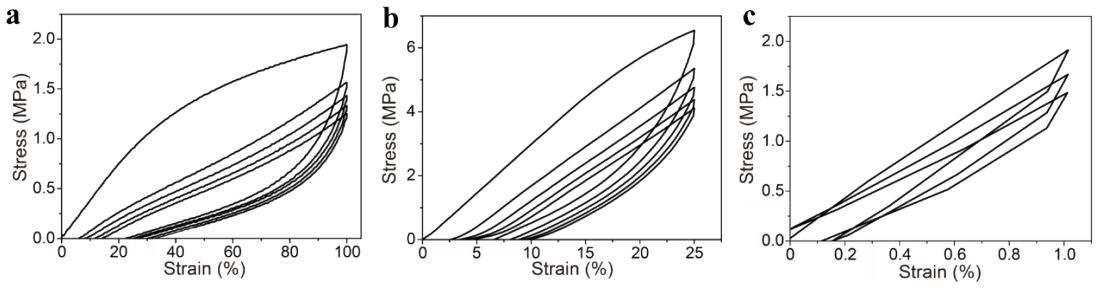

Figure S15. Cyclic stress-strain curves of TSE-4 (a), TSE-9 (b), and TSE-15 (c).

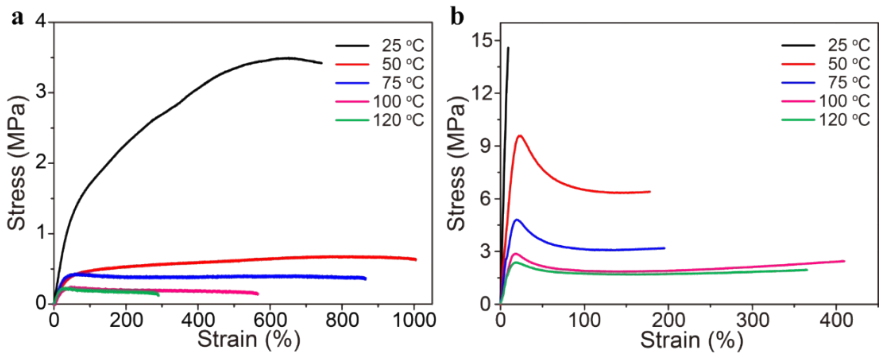

Figure S16. Stress-strain curves at the strain rate of 0.055 s^{-1} with different temperatures for TSE-4 (a), TSE-15 (b).

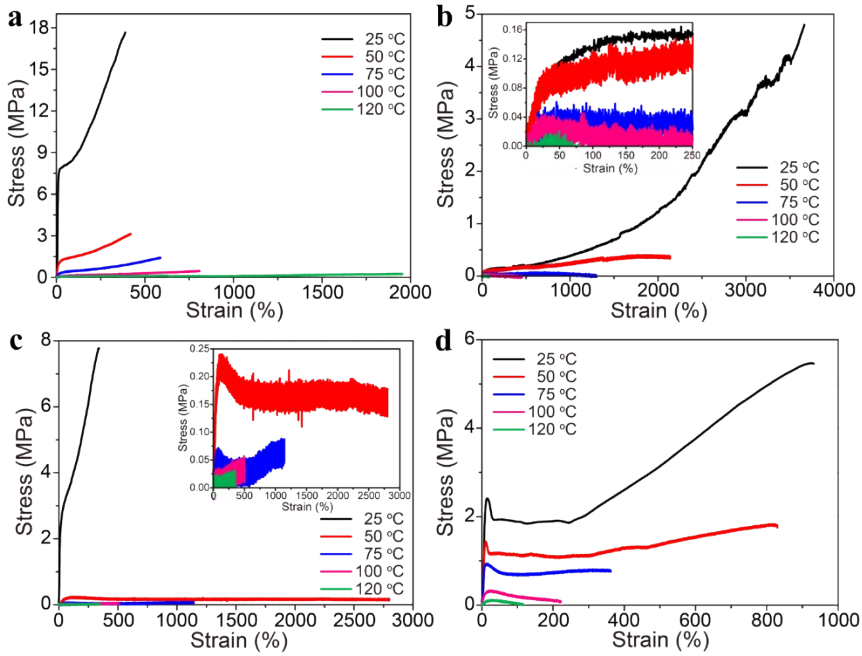

Figure S17. Stress-strain curves at the strain rate of 0.055 s^{-1} with different temperatures for ionic bonding elastomer (HiSHE-37, a), hydrogen bonding elastomer (p(BA-AM)-20, b), coordination bonding elastomer (EV-VP-$Cu_{1/24}$, c), and SBS (d).

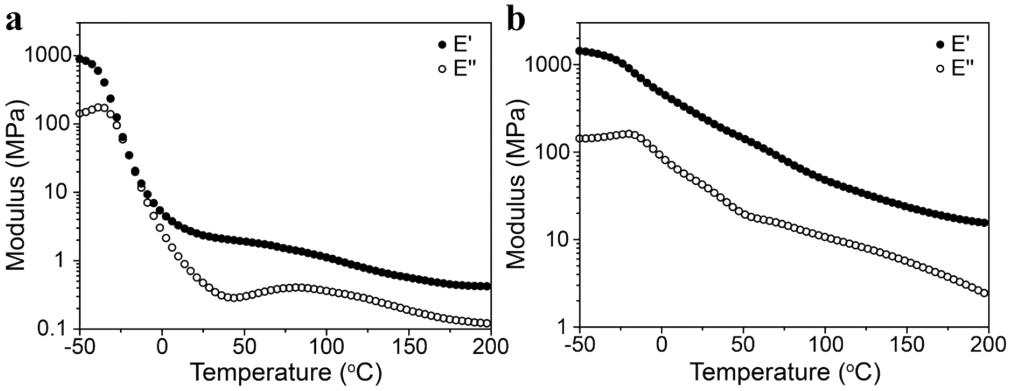

Figure S18. Storage and loss modulus curves of TSE-4 (a) and TSE-15 (b).

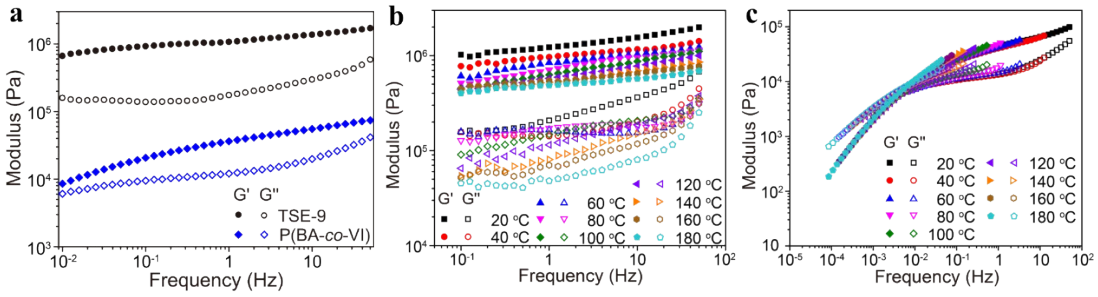

Figure S19. (a) Frequency dependence of storage modulus and loss modulus at 25 °C for TSE-9 and P(BA-*co*-VI). (b) Frequency dependence of storage modulus and loss modulus with different temperatures for TSE-9. (c) The master curves of P(BA-*co*-VI).

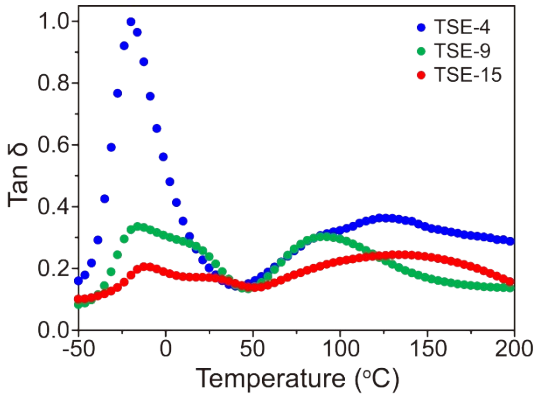

Figure S20. Tan δ curves of TSEs.

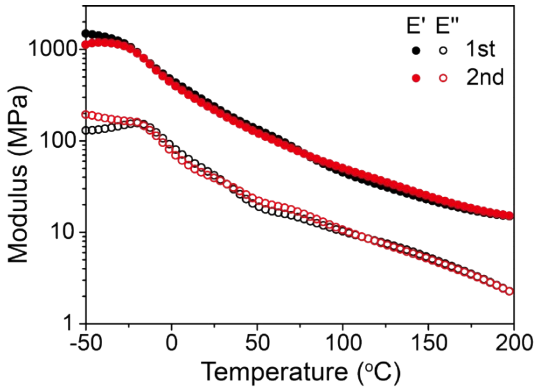

Figure S21. Storage and loss modulus curves of TSE-15 with repeated heat treatment.

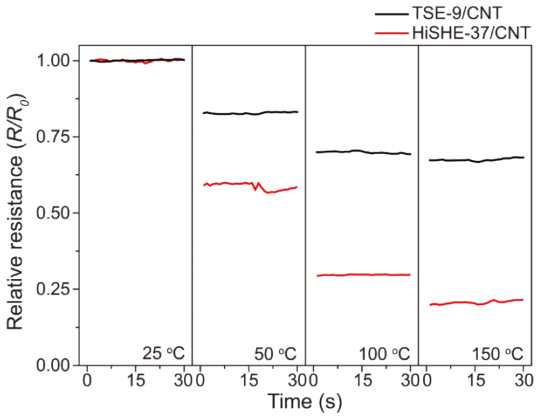

Figure S22. The relative resistance (R/R_0) of TSE-9/CNT and HiSHE-37/CNT at different temperatures.

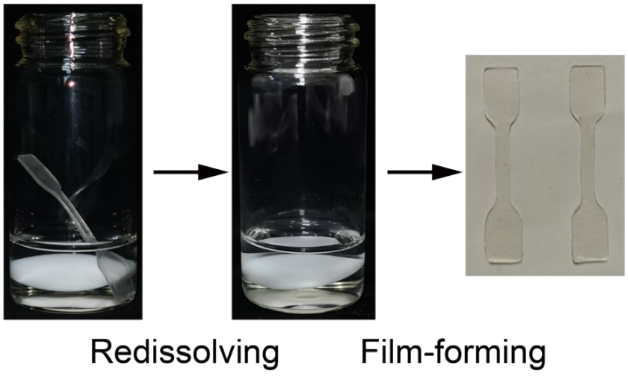

Figure S23. Redissolving and film-forming process of TSE-9.

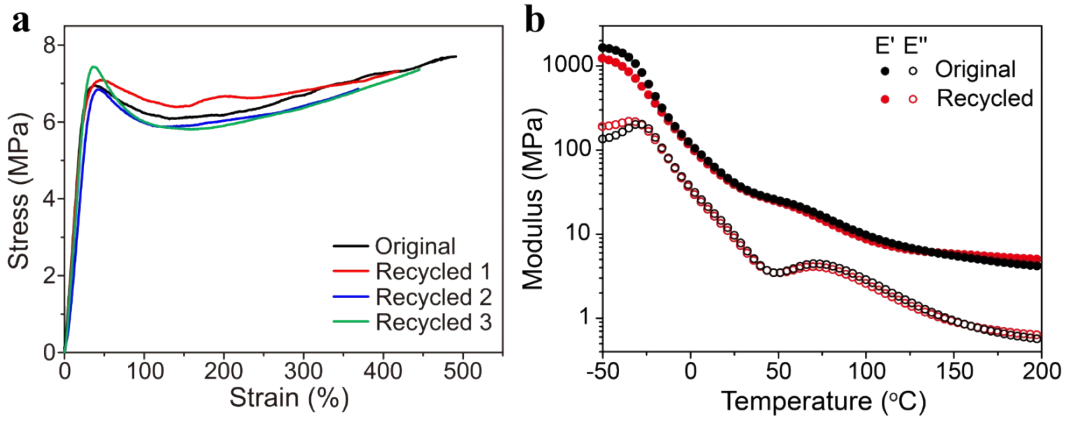

Figure S24. Recycled properties of TSEs: (a) Stress-strain curves for original and recycled TSE-9. (b) Storage and loss modulus curves of original and recycled TSE-9. TSEs show the good recyclability.

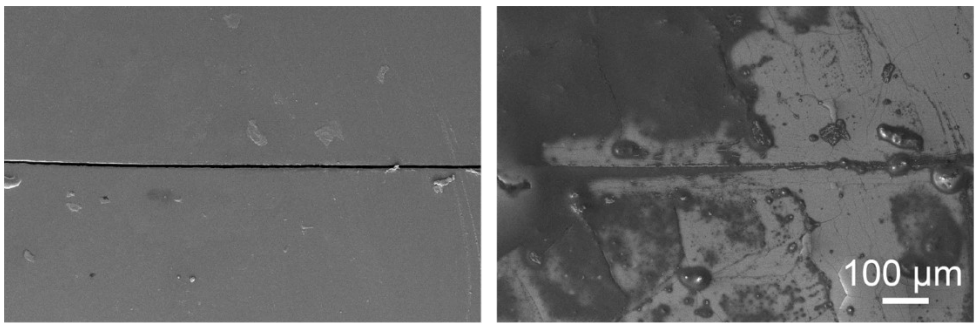

Figure S25. SEM images of mending process of TSE-9: the original state after cut (left) and the solvent-enabled healed state (right).

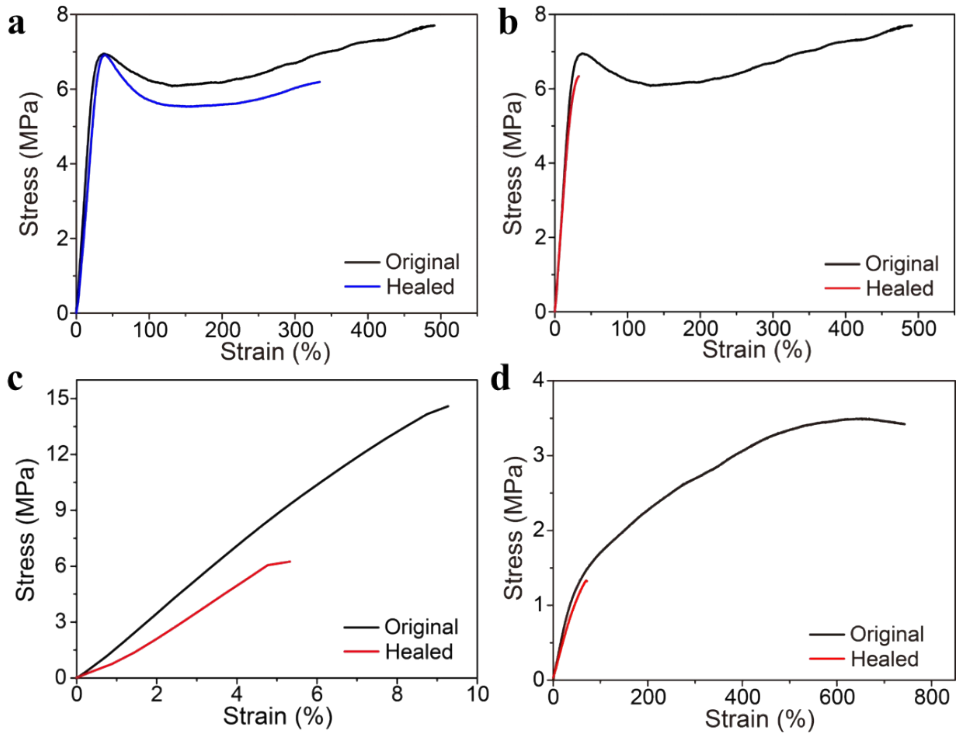

Figure S26. Stress-strain curves of the original samples and corresponding samples healed at room temperature for 24 h: TSE-9 with crack (a) and TSE-9 with fracture (b). Stress-strain curves of the uncut samples and corresponding cut samples healed at room temperature for 24 h: TSE-15 (c) and TSE-4 (d).

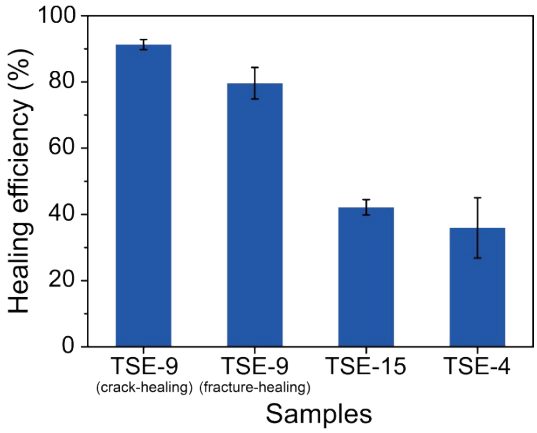

Figure S27. Healing efficiency after 24 h at room temperature for TSEs.

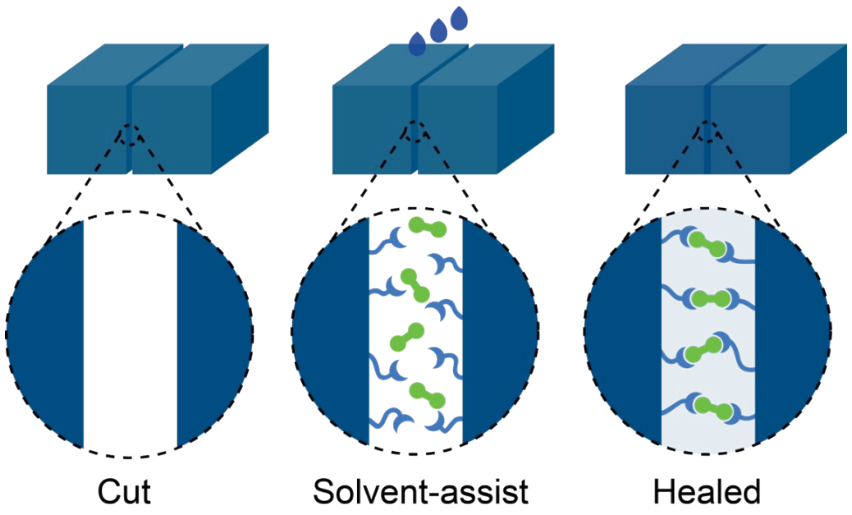

Figure S28. Schematic illustration of the solvent-enabled mending process: Free functional groups are generated with the assistance of solvent in the surface, and then boron dative bonds are reformed across the fracture.

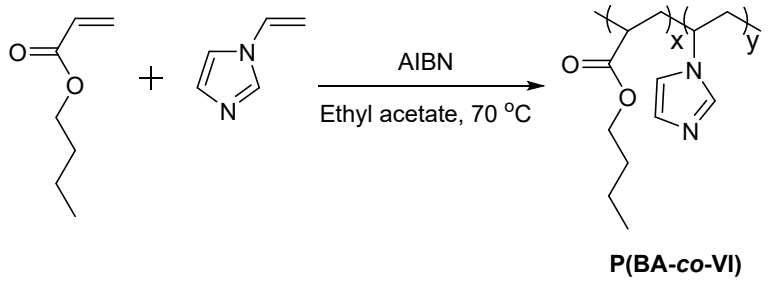

Scheme S1. Preparation of P(BA-*co*-VI).

Table S1. Characterizations of P(BA-*co*-VI).

P(BA-*co*-VI) species of sample	Feed molar ratio between VI and BA	Raw VI unit content (mol %)	Actual VI unit content (mol %)[a]	Mn (g/mol)	Mw (g/mol)	PDI
TSE-15	1 : 6	14.2	15.1	91430	219848	2.40
TSE-9	1 : 14	6.6	9.2	131000	341013	2.11
TSE-4	1 : 24	4.0	3.8	262132	499684	1.91

a. The actual VPBA unit contents were calculated from ^{1}H NMR spectra

Movie S1. The appearance and elasticity of TSE-9 at 25 and 130 ^{o}C.

Movie S2. The appearance of SBS at 25 and 130 ^{o}C.

References

1. Grimme, S.; Antony, J.; Ehrlich, S.; Krieg, H., A consistent and accurate ab initio parametrization of density functional dispersion correction (DFT-D) for the 94 elements H-Pu. *J. Chem. Phys.* **2010,** *132* (15), 154104.
2. Xu, S.; He, T.; Li, J.; Huang, Z.; Hu, C., Enantioselective synthesis of D-lactic acid via chemocatalysis using MgO: Experimental and molecular-based rationalization of the triose's reactivity and preliminary insights with raw biomass. *Appl. Catal. B Environ.* **2021,** *292*, 120145.
3. Krishnan, R.; Binkley, J. S.; Seeger, R.; Pople, J. A., Self-consistent molecular orbital methods. XX. A basis set for correlated wave functions. *J. Chem. Phys.* **1980,** *72* (1), 650-654.
4. Reed, A. E.; Curtiss, L. A.; Weinhold, F., Intermolecular interactions from a natural bond orbital, donor-acceptor viewpoint. *Chem. Rev.* **1988,** *88* (6), 899-926.
5. Lai, J.-C.; Mei, J.-F.; Jia, X.-Y.; Li, C.-H.; You, X.-Z.; Bao, Z., A Stiff and Healable Polymer Based on Dynamic-Covalent Boroxine Bonds. *Adv. Mater.* **2016,** *28* (37), 8277-8282.
6. Erdogdu, Y.; Tahir Güllüoğlu, M.; Kurt, M., DFT, FT-Raman, FT-IR and NMR studies of 2-fluorophenylboronic acid. *J. Raman Spectrosc.* **2009,** *40* (11), 1615-1623.
7. Foran, G. Y.; Harris, K. J.; Brook, M. A.; Macphail, B.; Goward, G. R., Solid State NMR Study of Boron Coordination Environments in Silicone Boronate (SiBA) Polymers. *Macromolecules* **2019,** *52* (3), 1055-1064.
8. Hušák, M.; Jegorov, A.; Rohlíček, J.; Fitch, A.; Czernek, J.; Kobera, L.; Brus, J., Determining the Crystal Structures of Peptide Analogs of Boronic Acid in the Absence of Single Crystals: Intricate Motifs of Ixazomib Citrate Revealed by XRPD Guided by ss-NMR. *Cryst. Growth Des.* **2018,** *18* (6), 3616-3625.
9. Hwang, S.-J.; Chen, C.-Y.; Zones, S. I., Boron Sites in Borosilicate Zeolites at Various Stages of Hydration Studied by Solid State NMR Spectroscopy. *J. Phys. Chem. B* **2004,** *108* (48), 18535-18546.
10. Huang, H.; Liu, M.; Luo, S.; Wang, K.; Wan, Q.; Deng, F.; Xu, D.; Zhang, X.; Wei, Y., One-step preparation of AIE-active dextran via formation of phenyl borate and their bioimaging application. *Chem. Eng. J.* **2016,** *304*, 149-155.
11. Qin, Y.; Cui, C.; Jäkle, F., Silylated Initiators for the Efficient Preparation of Borane-End-Functionalized Polymers via ATRP. *Macromolecules* **2007,** *40* (5), 1413-1420.
12. De, P.; Gondi, S. R.; Roy, D.; Sumerlin, B. S., Boronic Acid-Terminated Polymers: Synthesis by RAFT and Subsequent Supramolecular and Dynamic Covalent Self-Assembly. *Macromolecules* **2009,** *42* (15), 5614-5621.
13. Han, L. M.; Timmons, R. B.; Bogdal, D.; Pielichowski, J., Ring Retention via Pulsed Plasma Polymerization of Heterocyclic Aromatic Compounds. *Chem. Mater.* **1998,** *10* (5), 1422-1429.
14. Yu, C.; Wang, C.-F.; Chen, S., Robust Self-Healing Host–Guest Gels from Magnetocaloric Radical Polymerization. *Adv. Funct. Mater.* **2014,** *24* (9), 1235-1242.
15. Zhan, K.; Kim, C.; Sung, K.; Ejima, H.; Yoshie, N., Tunicate-Inspired Gallol Polymers for Underwater Adhesive: A Comparative Study of Catechol and Gallol. *Biomacromolecules* **2017,** *18* (9), 2959-2966.
16. Althues, H.; Simon, P.; Kaskel, S., Transparent and luminescent YVO4 : Eu/polymer nanocomposites prepared by in situ polymerization. *J. Mater. Chem.* **2007,** *17* (8), 758-765.
17. Shundo, A.; Aoki, M.; Yamamoto, S.; Tanaka, K., Effect of Cross-Linking Density on

Horizontal and Vertical Shift Factors in Linear Viscoelastic Functions of Epoxy Resins. *Macromolecules* **2021,** *54* (20), 9618-9624.